MATERIALS SCIENCE

Ion transport and ultra-efficient osmotic power generation in boron nitride nanotube porins

Zhongwu Li[1], Alex T. Hall[2], Yaqing Wang[1], Yuhao Li[1], Dana O. Byrne[3,4], Lyndsey R. Scammell[5], R. Roy Whitney[5], Frances I. Allen[4,6], John Cumings[2], Aleksandr Noy[1,7]*

Nanotube porins form transmembrane nanomaterial-derived scaffolds that mimic the geometry and functionality of biological membrane channels. We report synthesis, transport properties, and osmotic energy harvesting performance of another member of the nanotube porin family: boron nitride nanotube porins (BNNTPs). Cryo–transmission electron microscopy imaging, liposome transport assays, and DNA translocation experiments show that BNNTPs reconstitute into lipid membranes to form functional channels of ~2-nm diameter. Ion transport studies reveal ion conductance characteristics of individual BNNTPs, which show an unusual $C^{1/4}$ scaling with ion concentration and pronounced pH sensitivity. Reversal potential measurements indicate that BNNTPs have strong cation selectivity at neutral pH, attributable to the high negative charge on the channel. BNNTPs also deliver very large power density up to 12 kW/m^2 in the osmotic gradient transport experiments at neutral pH, surpassing that of other BNNT-based devices by two orders of magnitude under similar conditions. Our results suggest that BNNTPs are a promising platform for mass transport and osmotic power generation.

INTRODUCTION

Biological membrane channels play a crucial role in various processes related to energy conversion and molecular separation in living systems, regulating the transport of ions and molecules across membranes (*1*, *2*). Nature has mastered manipulation of the geometry, chemical functionality, and transport mechanisms in these channels to achieve astonishingly efficient and selective transport characteristics (*3*). The remarkable performance of biological membrane pores has spurred the development of biomimetic and bioinspired nanochannels, which include protein, peptide, DNA-based channels, and other synthetic analogs that aim to replicate the unique transport characteristics of their biological counterparts (*4*, *5*). Many bioinspired nanofluidic channels have shown fascinating ion transport properties (*6*). Quasi–zero-dimensional nanopores in atomically thin MoS_2 have demonstrated strong ion gating and selective transport performance due to their inherent surface charge (*7*, *8*). Two-dimensional graphene nanochannels show ion selectivity that goes beyond mere steric sieving effects (*9*).

Nanofluidic channels tailored for specific ion transport dynamics also open exciting possibilities for harvesting the energy of osmotic gradients and converting it to electric power (*10*, *11*). Osmotic power is generated when a strongly ion-selective fluidic channel connects two reservoirs of different salinity. Spatial confinement and surface charge are the two critical factors that determine osmotic power generation performance of a membrane pore (*12*, *13*). Channels wider than Debye length cannot deliver the required ion selectivity. A high surface charge of the nanochannel wall is also crucial because it creates conditions for co-ion exclusion that enhances the channel selectivity and osmotic current. It is not unexpected that nanopores and nanochannels that combine high surface charge and strong spatial confinement have been at the forefront of osmotic energy harvesting efforts. One-dimensional nanotube scaffolds, such as carbon nanotubes (CNTs) and boron nitride nanotubes (BNNTs), represent a particularly compelling scaffold for creating such platforms. These materials offer the multiple advantages of precise geometry that defines strong spatial confinement, robust structure, and clean regular surfaces with defined chemical and electronic characteristics, which in turn can determine transport and ion rejection behavior (*6*). In particular, BNNTs have stood out in these efforts because of their unique surface morphology and massive surface charge (*14*–*19*), stemming from the boric acid chemical ionization equilibrium (*20*–*22*).

Pioneering work by Siria *et al.* (*15*) demonstrated BNNT's potential for osmotic power generation by showing that devices made with BNNT, with diameters ranging from 30 to 80 nm, can achieve outputs as high as ~4 kW/m^2, which surpassed that of traditional ion exchange membranes used in reverse electrodialysis (<5 W/m^2) (*12*, *23*, *24*). Recent work by Pendse *et al.* (*17*) also showed that the membranes composed of 30-nm-diameter BNNTs can generate high osmotic power under the salt concentration gradient. Cetindag *et al.* (*18*) also reported that macroscopic arrays of aligned BNNTs in 3- or 12-nm diameter in a salt concentration gradient produced osmotic-power densities up to ~10 kW/m^2 per pore. However, these studies mainly focused on micrometer-long BNNTs with large diameters that operated under extreme conditions, such as very high pH levels and salinity gradients, which remain impractical. In contrast, shorter BNNT channels would offer numerous advantages, including reduced electrical and transport resistance (*13*, *25*). The critical role of the channel length in achieving higher osmotic power output has been demonstrated when a nanopore in single-layer MoS_2 (*8*) achieved exceptionally high osmotic power characteristics. While incorporating very short nanotube channels in a measurement platform is difficult, the nanotube porin platform provides a particularly facile approach. This strategy, which embeds short segments of nanotubes in lipid bilayer membranes, was first demonstrated with CNT porins

[1]Materials Science Division, Physical and Life Sciences Directorate, Lawrence Livermore National Laboratory, 7000 East Avenue, Livermore, CA 94550, USA. [2]Department of Materials Science and Engineering, University of Maryland, College Park, MD 20742, USA. [3]Department of Chemistry, University of California, Berkeley, Berkeley, CA 94720, USA. [4]National Center for Electron Microscopy, Molecular Foundry, Lawrence Berkeley National Laboratory, Berkeley, CA 94720, USA. [5]BNNT Materials LLC, Newport News, VA 23606, USA. [6]Department of Materials Science and Engineering, University of California Berkeley, Berkeley, CA 94720, USA. [7]School of Natural Sciences, University of California, Merced, Merced, CA 93434, USA.
*Corresponding author. Email: noy1@llnl.gov

(CNTPs) (*26*, *27*). BNNTs represent another potential candidate for creating bioinspired membrane channels, particularly those with high surface charge to enable enhanced selectivity and efficient osmotic power conversion.

Here, we report the synthesis of BNNT porins (BNNTPs) and their incorporation into lipid membranes to expand the nanotube porin platform. Cryogenic transmission electron microscopy (cryo-TEM) imaging and liposome transport assays confirm that BNNTPs incorporate into the lipid bilayers and create passive transmembrane pores. Single-channel conductance measurements using droplet interface bilayers (DIBs) reveal that BNNTPs have distinct ion transport properties and ion conductance scaling. Notably, we found that these nanotube porin species exhibit strong cation selectivity above pH 4, which allows them to achieve very high osmotic power generation density of ~12 kW/m^2 under just a 10-fold salinity gradient at neutral pH, a performance that is two orders of magnitude higher than what has been reported for other BNNT systems under similar conditions.

RESULTS

We created BNNTPs using modified lipid-assisted sonochemical cutting of macroscopically long multiwall BNNTs (Fig. 1A), in an adaptation of the procedure that we previously reported for CNTP synthesis (*28*). Our approach diverges from the conventional surfactant-assisted BNNT dispersion techniques (*29*, *30*), which would introduce substances that potentially compromise the stability of lipid membranes. Instead, we opted to disperse BNNTs from their initial "puffball" form in a suspension of 1,2-dioleoyl-*sn*-glycero-3-phosphocholine (DOPC) lipids. This suspension, as revealed by helium ion microscopy (HIM) imaging (Fig. 1Aii), contained micrometer-long BNNTs that still show some degree of aggregation. Subsequent probe sonication, followed by removal of longer BNNT fragments by centrifugation, further separated the BNNTs from the bundles and eventually created notably shorter BNNT segments coated by lipid molecules, i.e., BNNTPs (Fig. 1Aiii), which could then be incorporated into liposomes (Fig. 1Aiv). High-resolution transmission electron microscopy (HR-TEM) analysis (Fig. 1B and fig. S1), indicates that the BNNTPs have an average inner diameter of ~2.1 nm. This dimension is consistent with the average height of ~2.8 nm observed via atomic force microscopy (AFM) (fig. S2), accounting for the typical double to triple-walled structure commonly found for as-synthesized BNNTs. As expected for the BN nanotube surface, zeta-potential measurements indicated that as-synthesized BNNTPs have strong negative surface charge (fig. S3), consistent with the literature reports (*15*, *18*).

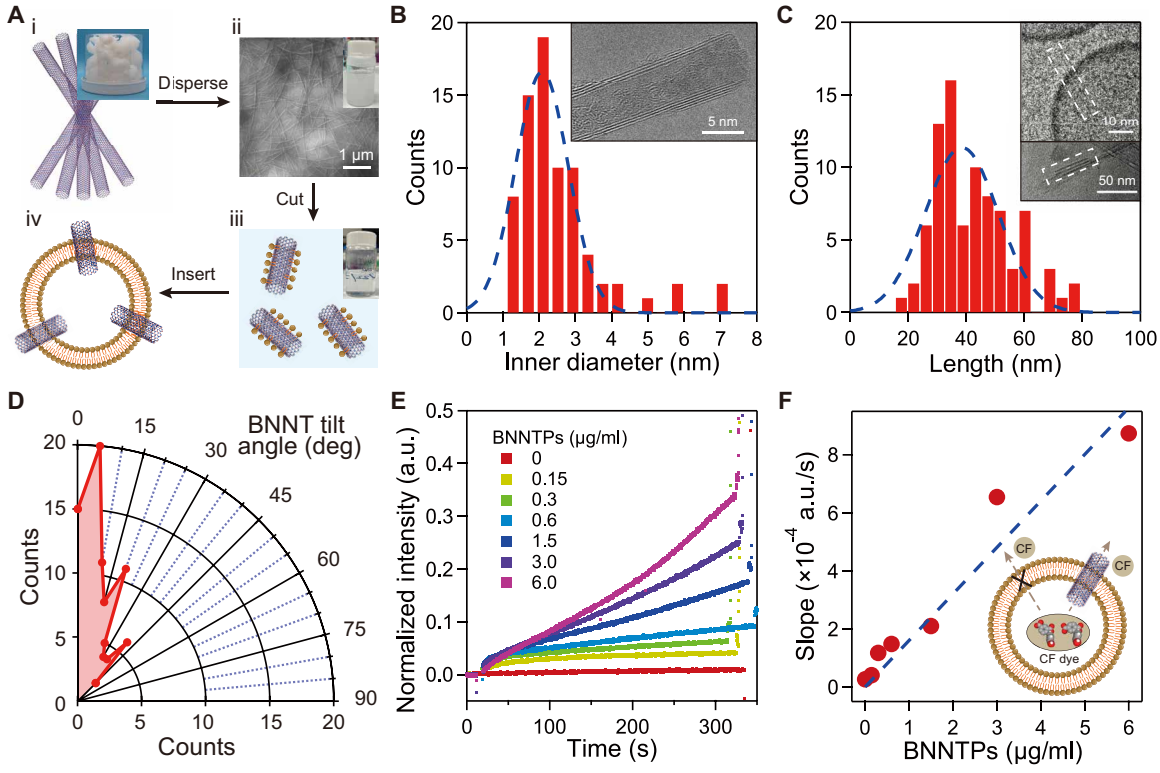

Fig. 1. Synthesis, characterization, and incorporation of BNNTPs. (**A**) Schematic showing BNNTP preparation. i. Schematic of uncut BNNTs and a photograph of raw BNNTs in "puffball" status. ii. HIM imaging of dried BNNTs after dispersing with lipids in water and a photograph of uncut BNNT-lipids solution. iii. Schematic of cut, lipid-stabilized BNNT segments and a photograph of a cut BNNT suspension. iv. Schematic showing BNNTP incorporation into liposomes. (**B**) Histogram of the inner diameters of cut BNNT fragments measured with HR-TEM and a Gaussian fit to the data. Most BNNTPs show two to three walls. Inset: HR-TEM image of a single BNNTP. (**C**) Histogram of the lengths of the BNNTPs inserted into the lipid membrane and a Gaussian fit to the data. Inset: Cryo-TEM image of single BNNTP incorporated in the liposome bilayer (top) and individual BNNTPs (bottom). (**D**) Radius plot of the histogram of BNNTP tilt angles measured relative to the axis normal to the bilayer plane. (**E**) Time traces of the normalized fluorescence intensity of self-quenching CF dye after additions of BNNTPs to different concentrations. (**F**) Initial slopes of CF dye fluorescence intensity plotted as a function of BNNTP concentration. Dashed line is a linear fit to the data. Inset: Schematic illustration of CF dye leakage assay for qualitatively probing channel size formed by BNNTPs.

Cryo-TEM imaging of BNNTPs reconstituted into large unilamellar vesicles (LUVs) provided further insights into their structure. Cryo-TEM images showed short BNNT fragments seamlessly integrated into the lipid bilayers (Fig. 1C, inset and fig. S4). Statistical analysis of the cryo-TEM images revealed that the lengths of the cut BNNTs incorporated into the lipid vesicles followed a normal distribution, with an average of 38.4 ± 2.2 nm. This is longer than the cut CNTs (~10 nm) (*28*), a difference attributed to the multiwall nature of BNNTs, yet markedly shorter than the lengths typically achieved through surfactant-assisted cutting (*29*). Despite their length greatly exceeding the typical ~5-nm lipid bilayer thickness, the BNNTPs predominantly orient themselves perpendicularly to the plane of the membrane. A histogram of the membrane tilt angles (Fig. 1D) shows that most BNNTPs exhibit only minimal tilt, deviating by only about 5° from the membrane normal.

We assessed the incorporation, and pore-forming activity of the BNNTPs, with a 5(6)-carboxyfluorescein (CF) dye leakage assay (*31*) (Fig. 1, E and F). This assay is based on monitoring the fluorescence of a CF dye, a ~1-nm molecule that is sequestered in the vesicle lumen in a self-quenching concentration above 50 mM. If CF molecules trapped inside the LUVs escape through channels larger than 1 nm (fig. S5), they immediately dequench, leading to an increase in fluorescence intensity. When we added BNNTPs to CF-encapsulating LUVs, we observed a strong increase in fluorescence, indicating that CF dyes were escaping out of the vesicles. The initial slopes of the fluorescence intensity kinetic curves correlated directly with the quantity of BNNTPs added (Fig. 1F), strongly indicating that BNNTPs were indeed inducing the dye leakage. These experiments confirm that BNNTPs spontaneously incorporate into the lipid vesicles and form channels of larger than 1-nm size, an observation that is fully consistent with the TEM results.

We explored the ion transport in BNNTPs with a DIB setup (*32*, *33*). In these experiments we placed two liquid droplets each encased in a monolayer of 1,2-diphytanoyl-*sn*-glycero-3-phosphocholine (DPhPC) lipid and filled with buffer into an oil bath. We then carefully brought the two monolayer-encased droplets together using a micromanipulator to form a small patch of lipid bilayer in the droplet contact zone (Fig. 2A). Each droplet also contained a small electrode that allowed us to record transmembrane ion current. This setup also allowed us to monitor the bilayer formation by observing capacitance current under a triangular voltage wave (fig. S6). From these measurements, we estimated the typical diameter of the bilayer patch at the droplet interface to be ~100 to 300 μm. Once formed, the bilayer was very stable even under a high voltage of 200 mV and was able to tolerate abrupt stepwise voltage changes (fig. S6). We further validated the performance of our DIB system by detecting

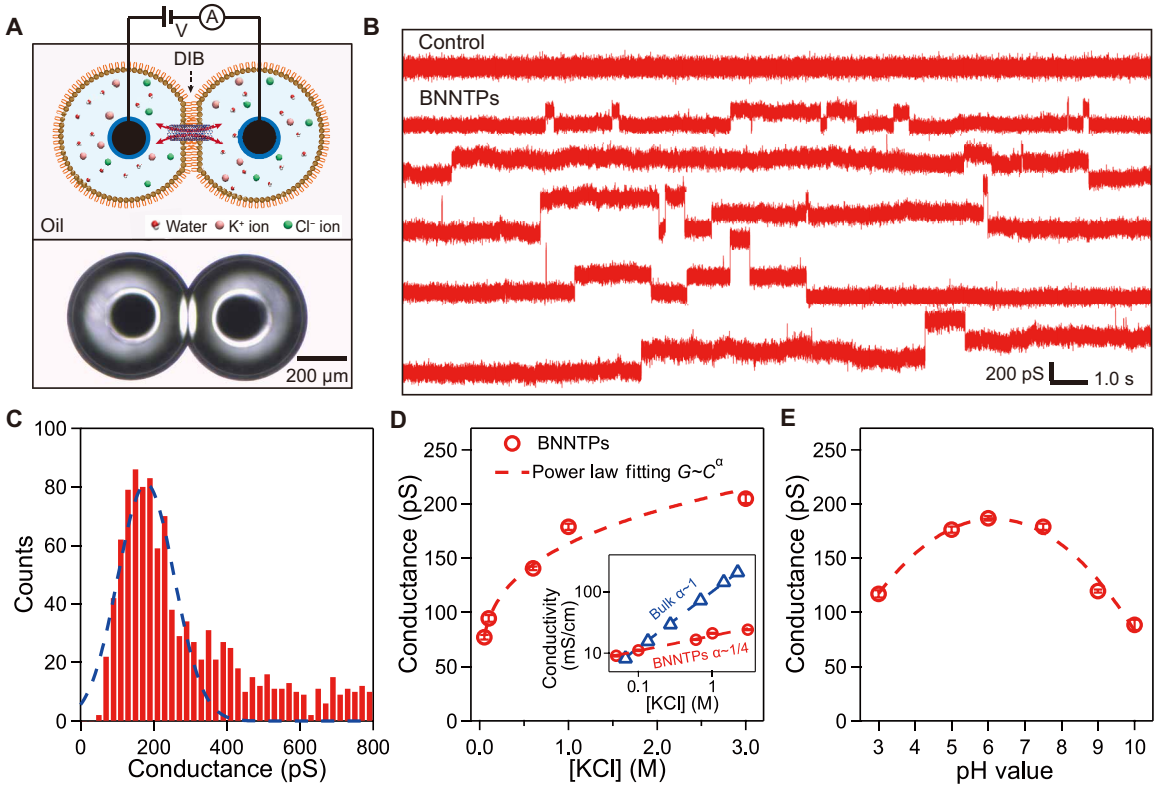

Fig. 2. Ion transport in individual BNNTPs. (**A**) Schematic illustration for single-channel recording of BNNTP conductance where an interface lipid bilayer formed between two droplets (top) and optical microscope image of hanging droplets with bilayer at the interface (bottom). (**B**) Representative conductance traces showing incorporation of BNNTPs into the lipid bilayer for 1 M KCl at pH 7.5. Control trace was recorded in absence of BNNTPs. (**C**) Histogram of BNNTP conductance values for 1 M KCl at pH 7.5. Dashed blue line is a Gaussian fit to the data. (**D**) Ion conductance of individual BNNTPs measured over a range of KCl concentrations at pH 7.5. Dashed line indicates fits to a power law. Inset: Ion conductivity versus KCl concentration for BNNTPs and bulk solutions (*35*) at pH 7.5. Dashed lines are best fits of the data to a power law. The ion conductivity of BNNTPs was determined from the ion conductance with $\kappa = G\left(\frac{4L}{\pi d^2} + \frac{1}{d}\right)$, where G is the conductance, L is the length, and d is the inner diameter of BNNTPs. (**E**) Ion conductance of individual BNNTPs measured over a range of pH for 1 M KCl. Dashed line is a guide to the eye.

the incorporation of α-hemolysin (α-HL) protein channels into the lipid bilayer (fig. S7). The ion conductance of α-HL in these experiments, ~0.98 nS in a 1 M KCl solution at pH 7.5, agrees with values reported in literature under similar conditions (*34*).

After introducing BNNTPs into the DIB system droplets, we observed a series of conductance jumps, corresponding to spontaneous incorporation of these porins into the membrane (Fig. 2B). A histogram of the conductance step values measured in these experiments (Fig. 2C) reveals a prominent peak at ~179 pS followed by a series of smaller conductance peaks at approximately double and triple of this value. While there were occasional conductance jumps registering higher than these values, these occurrences were relatively infrequent. Thus, we conclude that the main peak of the histogram corresponds to BNNTP single insertion events and the events with larger conductance values correspond to insertion of the BNNTP dimers and primers resulting from the aggregation of BNNTs. The conductance of BNNTPs was lower than values we reported previously for the slightly narrower (~1.5-nm diameter) and shorter CNTPs (*26*). This observation is not unexpected given not only the length difference but also the notable difference in surface properties, which could also influence ion transport behavior.

The relationship between the ion conductance of BNNTPs and ion concentration (Fig. 2D and figs. S8 and S9) reveals additional details of ion transport in BNNTPs. We observed a clear power-law dependence of BNNTP conductance on ion concentration, characterized by an exponent value of $\alpha \sim {}^{1}/_{4}$. This value deviates notably not only from the linear conductance dependence on ion concentration typically expected in bulk solutions (Fig. 2D, inset) (*35*), but also from the one-third and two-thirds power-law exponents reported for CNT channels (*36*, *37*).

Conductance characteristics of nanochannels can be complicated. Channels with fixed surface charge typically exhibit a conductance saturation at lower ionic strengths, indicating a transition from a bulk-dominated to a surface-dominated transport regime (*38*), where the ion transport becomes primarily driven by counterions accumulating near the charged surface. Secchi *et al.* (*36*) showed how this behavior can be modified by charge regulation at the channel wall, producing a scaling law of $\alpha \sim {}^{1}/_{3}$ in long wide CNTs. Manghi *et al.* subsequently expanded this model to include electroosmotic coupling producing the $\alpha \sim {}^{2}/_{3}$ dependence observed in larger diameter CNTPs (*37*, *39*). Further, Queralt-Martin *et al.* (*40*) reported that biological channels exhibit a range of power-law scaling exponents, from ${}^{1}/_{10}$ to ${}^{4}/_{5}$. Cui *et al.* (*41*) found that the ion conductance in ~2.2-nm-diameter CNTs has a $\alpha \sim {}^{1}/_{3}$ scaling for KCl while a $\alpha \sim {}^{1}/_{4}$ for NaCl and $\alpha \sim {}^{1}/_{10}$ for LiCl. Not only these exponents, but almost any power-law exponent ranging from $0 \leq \alpha < 1$, have been observed (*42*). Thus, the observation of a relatively low value of $\alpha \sim {}^{1}/_{4}$ for BNNTPs at low ion concentrations is not unexpected, indicating that ion conductance is strongly determined by the charge on the BN surface of the nanotube. We estimated the surface charge on the BNNTP surface using a charge regulation model (*36*, *43*) that assumes surface charge density versus salt concentration scaling of $\sigma(C) \propto C^{1/4}$ (fig. S10), as simple fixed charge model resulted in a poor fit. The surface charge density values derived from this fit exhibited an increase with ion concentration, reaching higher absolute values than the previously reported surface charge densities for BNNTs with larger diameters of 30 to 80 nm (*15*, *19*). We attribute these higher values to higher reactivity of the highly curved BNNTP walls.

However, the observation of a power-law dependence of the ion conductance at high ion concentrations (up to 3 M) in BNNTPs is unusual. Normally, screening of surface charges at the channel wall leads to a reduction in channel selectivity and the emergence of bulk conductance characteristics. In our experiments, BNNTPs presented an intriguing deviation from this norm. This behavior is also qualitatively different from the conductance saturation that we previously observed in 0.8-nm-diameter CNTPs where the ion conductance saturated above 0.25 M (*44*). This unusual persistence of the power law scaling in BNNTPs might stem from the high surface charge density of the narrow BNNTPs that may lead to the dominance of the surface conductance pathway at all ion concentrations that we have studied. This high surface charge could potentially lead to robust ion accumulations and attractions within the crowded channels, thereby increasing channel resistance. This behavior contrasts with the conductance properties of the weakly charged, smoother CNTs (*36*, *37*), as well as those of BNNTs of larger dimensions (*15*). We also found reduced ion conductivity in BNNTPs compared to the bulk solution value (Fig. 2D, inset), supporting this hypothesis.

We have also explored ion conductance dependence on solution pH values. When we adjusted the 1 M KCl solution pH from 3 to 7, the conductance of BNNTPs gradually increased. Intriguingly, as we increased the pH further, BNNTP ion conductance did not increase monotonically but instead showed a maximum at neutral pH values (Fig. 2E and fig. S11). A similar phenomenon was observed in two-dimensional charged graphene nanochannels (*43*). Several factors could be responsible for this suppression of ion transport in BNNTPs at high pH. We speculate that increased ion trapping in the highly charged BNNTP channel walls could be responsible for this effect (*45*, *46*). Other possible explanations could include the facilitated formation of ion pairs in small confined channels (*47*, *48*), an interplay between entropy and hydration energy in layered liquid structures (*49*), or the polarization of BNNT walls (*50*). This complexity necessitates further simulation work to fully unravel the underlying mechanism.

Verifying the precise pathway of ion transport is an important component of nanofluidic transport experiments. For the BNNTP system, it is also essential to confirm that ion transport occurs through the nanotubes themselves, rather than any gaps between the tube and the membrane (*51*). To verify this behavior, we studied the translocation of 50-nucleotide-long single-stranded DNA (50-nt ssDNA) oligomers through BNNTPs. Because of the high negative surface charge of the BNNTP wall, we had to conduct the experiments at ultrahigh KCl concentration of 3 M. When DNA was added to the cis droplet of our setup, which was grounded (Fig. 3A), we observed rapid conductance blockades indicating that individual ssDNA molecules were passing through the BNNTPs. While these blockades were prominent in 3 M KCl solutions at pH 7.5, we did not detect notable blockades at lower ion concentrations, which again was likely due to the repulsion between the negatively charged DNA and the highly negatively charged BNNTP wall that was insufficiently screened at this ion concentration. The conductance blockade values exhibited a normal distribution, centering around ~139 pS (Fig. 3, B and C), which corresponds to ~68% of the baseline BNNTP conductance. Given the physical dimensions of ssDNA, which has a diameter of ~1.2 nm, we estimated that this conductance blockade value corresponds to an effective ion transport diameter of ~1.5 nm. Compared to the average ~ 2.1-nm-diameter of BNNTPs established from the HR-TEM data, this value also implies the presence of an immobile

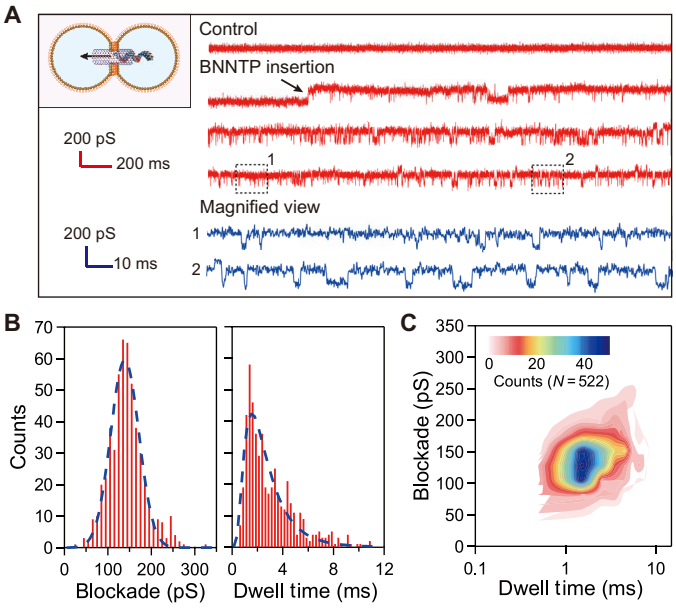

Fig. 3. DNA translocation through BNNTP ion channels. (**A**) Schematic showing the translocation of ssDNA through a BNNTP in the lipid bilayer. Conductance trace showing multiple transient blockades caused by 50-nt ssDNA translocation through the BNNTPs with magnified view (bottom). The top trace shows the control recorded in absence of BNNTPs. (Buffer: 3 M KCl, pH 7.5). (**B**) Histogram of conductance blockade levels for ssDNA translocation events and the dashed blue line is a Gaussian fit to the data (left). Histogram of dwell times for ssDNA translocation events and the dashed blue line is a log-normal fit to the data (right). (**C**) Contour plots of the conductance blockade versus dwell time.

ion layer of roughly 0.3 nm attracted to the charged walls, which is again consistent with the overall picture of a highly charged BNNT surface. The dwell times of DNA translocation followed a log-normal distribution, centering around ~1.55 ms, again confirming that the observed current blockades originated from the ssDNA chains transitioning through the BNNTP channel in the membrane. The average translocation time corresponds to an average DNA translocation speed of ~30 nt/ms, a rate that is comparable to that of biological nanopores (*52*). We observed a tight grouping of the ssDNA translocation events in the parameter space in the contour of conductance blockade versus dwell times (Fig. 3C), indicating a promising sensing ability of BNNTPs.

To explore the transport properties of BNNTPs further, we measured their ion selectivity using reversal potential experiments. These measurements involved exposing different sides of the BNNTPs to an ion concentration gradient across the two droplets (Fig. 4A, inset). Initially, as a control experiment, we verified that when both droplets contained identical ion concentration solutions, the BNNTP current-voltage (*I*-*V*) curves exhibited linear characteristics intersecting the origin (fig. S12). When we introduced asymmetric ion concentrations across the droplets, we observed a clear shift in the *I*-*V* curves (Fig. 4A and fig. S12), indicating that BNNTPs were indeed ion selective. Notably, the values of the zero-current potential were quite consistent across multiple experiments on membranes containing different numbers of BNNTPs, indicating that such ion selectivity was quite uniform across the BNNTP samples. The observed osmotic current values also agree with the values expected for ion current induced by osmotic forcing in a reverse electrodialysis–dominated transport regime (*24*, *53*), caused by high surface charge and strong Debye layer overlap in small-diameter BNNTPs.

Consistent with our expectations for a nanochannel with negatively charged walls, BNNTPs showed notable preference for K^+ ions over Cl^- ions at pH 7.5 (Fig. 4B). This cation permselectivity increased with decreasing ion concentration, ranging from ~0.3 at a high concentration of 3 M to nearly complete (1.0) at a lower concentration of 0.1 M. Particularly noteworthy was the behavior at concentrations below 0.2 M, where BNNTPs exhibited near perfect cation (K^+) selectivity. BNNTPs exhibited a K^+/Cl^- selectivity ratio (SR) of 7.4 at pH 7.5 at the typical seawater salinity level of 0.6 M (Fig. 4B, inset). This level of selectivity is notably higher compared to that of biological α-HL nanopores (SR ~ 0.8) (*54*) and CNTPs (SR ~ 1.5) (*37*) of similar diameter. Even in environments with higher KCl concentrations, such as 1 M and 3 M when the Debye length is slightly smaller than the radius of the BNNTPs and the surface charges should be strongly screened, BNNTPs continue to show a clear, though weaker, preference for K^+ ion selectivity over Cl^- ion (Fig. 4B). This sustained ion selectivity could be attributed to the induced diffusio-osmosis within the charged channels, as discussed in previous studies (*15*, *18*, *41*).

Given the high surface charge of the BNNTP wall, we can attribute this high K^+ ion selectivity of the BNNTPs to the Donnan exclusion effect. To validate this hypothesis, we conducted selectivity measurements at different pH levels, while keeping the salt concentrations constant (Fig. 4C and fig. S13). We observed a strong dependence of both the K^+ ion transference number and K^+/Cl^- ion permselectivity on the pH of the solutions. The K^+/Cl^- ion selectivity increased with pH, exhibiting the most substantial change between pH 3 and pH 5, and stabilizing in a plateau-like dependence across a wide pH range from 5 to 10. Specifically, the K^+ ion selectivity observed in neutral and basic conditions transitions to Cl^- ion selectivity in acidic solutions. This marked pH dependence parallels similar behaviors reported in biological OmpF channels (*55*, *56*), suggesting that the charged groups on the surface of the channel were being titrated. Supporting this notion, simulation studies (*20*–*22*) have indicated that the source of surface charges on BNNTs can be traced to the chemisorption of hydroxyl groups (OH^-) on the BN surface, $BN_3 + H_2O \rightleftharpoons BN_3\text{-}OH^- + H^+$, following a reaction mechanism similar to that of boric acid, as described by the Henderson-Hasselbalch equation (*57*, *58*). This observation implies that the ionization of boric acid groups is indeed responsible for the observed K^+ ion selectivity in BNNTPs. Fitting the K^+ ion transference number dependence on the pH values to a pH calibration equation (Fig. 4C) further confirms this conclusion, producing a BNNTP pK_a (where K_a is the acid dissociation constant) value of ~3.7. This value is notably lower than the pK_a ~ 5.5 found for BNNTs with larger diameters of 30 to 80 nm (*15*, *20*), suggesting enhanced reactivity of the charge groups in more confined channels and highlighting distinct surface properties of the BNNTPs.

The exceptional ion selectivity of BNNTPs holds high promise for advancing osmotic power generation approaches. In our study, we measured the maximum power output achievable by BNNTPs (fig. S14) and found that it can reach ~0.05 pW, depending on the ion concentration gradient and pH levels. To contextualize this finding, we assessed the osmotic power generation relative to the cross-sectional area of a single BNNTP (Fig. 4D and figs. S14 and S15), a common figure of merit in osmotic power research. Our results

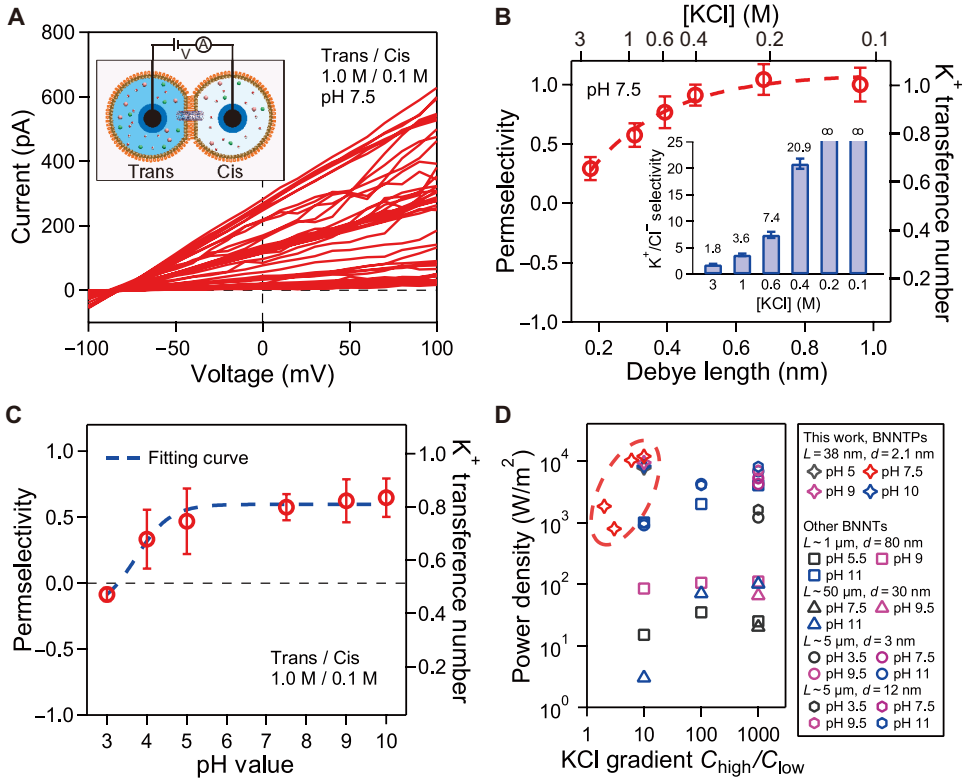

Fig. 4. Ion selectivity and osmotic power generation in BNNTPs. (**A**) *I-V* curves for different number of BNNTPs inserted into the membrane recorded for trans (1 M)/cis (0.1 M) KCl at pH 7.5. Inset: Schematic of the reversal potential measurements with asymmetric salt concentrations in two droplets. Transference number, permselectivity, and selectivity values were determined from the zero current potentials after subtracting the corresponding electrode redox potential. (**B**) K^+ ion transference number and K^+/Cl^- ion permselectivity values at pH 7.5 plotted as a function of the Debye length for different KCl concentrations in the high-salt droplet. Dashed line is a guide to the eye. Inset, K^+/Cl^- ion selectivity values at pH 7.5 as a function of the KCl concentration. (**C**) K^+ ion transference number and K^+/Cl^- ion permselectivity values plotted as a function of pH, where the KCl concentrations in the high-salt droplet and low-salt droplet are held at fixed values (1 M / 0.1 M KCl). Dashed blue line is best fit of K^+ transference number to a pH titration function: $t_+ = B_0 + B_1 \frac{10^{-pKa}}{10^{-pH} + 10^{-pKa}}$, where B_0 and B_1 are constants. (**D**) Osmotic power generation performance of BNNTPs compared with the reported larger BNNTs in terms of power density for different pH and salinity gradients. The power density values are calculated on the basis of power per unit pore surface area. The power density values of other larger BNNTs previously reported are taken from Siria *et al.* (*15*) (*L* ~ 1 μm, *d* = 80 nm), Pendse *et al.* (*17*) (*L* ~ 50 μm, *d* = 30 nm), and Cetindag *et al.* (*18*) (*L* ~ 5 μm, *d* = 3 nm, and *d* = 12 nm).

indicate that the power density of BNNTPs can attain levels as high as ~12 kW/m^2, with an energy conversion efficiency of ~16% (the theoretical maximum is 50%). Notably, this performance surpasses that of other BNNTs with larger sizes. For instance, the power density of BNNTPs exceeds that of BNNTs of 5 μm long and 12 nm in diameter by ~1.5 times and those 5 μm long and 3 nm in diameter by ~3 times (*18*). The power density is also ~3 times higher than BNNTs that are ~1 μm long and 80 nm in diameter (*15*) and ~2 orders of magnitude greater than BNNTs that are ~50 μm long and 30 nm in diameter (*17*). It is important to note that MoS_2 nanopores (*8*), with their atomic thickness of ~0.6 nm, showed even higher single-pore power densities (~100 kW/m^2), which could be attributed to their ultrathin structure. However, it is also important to consider the conditions under which these measurements were made. The power densities for larger-size BNNTs in previous studies (*15*, *17*, *18*) were obtained under extreme conditions of a 1000-fold salinity gradient at a high pH of 11. In contrast, our measurements for BNNTP power generation were conducted under a more moderate and practically feasible 10-fold salinity gradient at a neutral pH of 7.5, making our findings potentially more relevant for practical applications in harvesting blue energy. When comparing performance under identical conditions of a 10-fold salinity gradient at neutral pH, the power generation of BNNTPs is notably higher, up to two orders of magnitude greater than that of larger BNNTs. We can then estimate that a membrane with just ~0.03% pore density should be able to achieve power density that meets the commercialization benchmark of ~5 W/m^2 (*12*, *23*, *24*).

DISCUSSION

In summary, we have successfully fabricated BNNTPs and demonstrated their spontaneous incorporation into lipid membranes to create biomimetic nanochannels for efficient ion and molecular transport. Our ~38-nm-long BNNTPs exhibit superior ion conductance compared to macroscopically long BNNTs and demonstrate a $C^{1/4}$ scaling characteristic with ion concentration. Compared to CNTPs of similar dimensions, these ~2.1-nm-diameter channels show very high levels of cation selectivity, attributable to their high surface charges at neutral pH. This selectivity also results in exceptionally high osmotic power generation density, reaching up to ~12 kW/m^2 at neutral pH with just 10-fold salinity gradient. This performance surpasses existing power densities of traditional ion exchange membranes

(*12*, *23*, *24*) by several orders of magnitude and exceeds the efficacy of larger BNNTs by ~2 orders of magnitude under similar conditions (*15*, *17*, *18*).

Our results not only highlight the unique properties of BNNTPs but also point to the complex dynamics of ion transport through nanoscale channels. Understanding this dynamics is crucial for the advancement of nanofluidics and could have notbale implications for the development of next-generation membrane technologies. Our research underscores the utility of BNNTPs for harvesting "blue" energy from natural salinity gradients. Even though BNNT synthesis technology advances and ongoing reductions in membrane fabrication costs point to increased feasibility of large-scale energy conversion using BNNTPs (*59*, *60*), the real-world applicability and commercial viability will still need to be evaluated by detailed technoeconomic analysis (*53*, *61*, *62*). Last, the ease of incorporating BNNTPs into lipid membranes opens avenues for their application in physiological environments, enhancing the energy efficiency of biohybrid interfaces, implants, synthetic tissues, and microrobotic systems.

MATERIALS AND METHODS

Materials

The purified bulk BNNTs were provided by BNNT LLC, USA. BNNTs were synthesized with the high-temperature high-pressure method that preferentially produces two to three walled nanotubes. Both DOPC and DPhPC were sourced from Avanti Polar Lipids Inc., USA. 5(6)-CF, potassium chloride (KCl), sodium chloride (NaCl), tris base (tris), EDTA, Hepes, and α-HL from *Staphylococcus aureus*, alongside hexadecane, low-melt agarose gel, Sepharose CL-6B, and Triton X-100, were sourced from Sigma-Aldrich, USA. Short ssDNA oligonucleotides (50-adenine) were purchased from Integrated DNA Technologies Inc., USA.

BNNTP fabrication

BNNTPs were synthesized using a methodology adapted from the established protocols for CNTP synthesis (*28*). In brief, 36 mg of DOPC lipids in chloroform was added to a 20-ml glass scintillation vial. The chloroform was then evaporated for a duration of 10 min on a rotary evaporator, and the sample was dried overnight in a vacuum desiccator to ensure complete removal of residual solvent. Following this, ~0.8 mg of unprocessed BNNT material and 14 ml of deionized (DI) water were added to the vial and mixed with the dried lipid film. The resultant mixture underwent stirring at a speed of 1200 rpm for 4 hours, followed by 1 hour of bath sonication to ensure effective BNNT dispersion. The mixture was then processed with a probe sonicator (QSonica) for 16 hours to ensure BNNT fragmentation. Cut BNNTs were then centrifuged at 10,300*g* for 1 hour at 20°C using an Allegra X-30R centrifuge (Beckman Coulter). After centrifugation, the supernatant, rich in BNNTPs, was extracted with a glass pipette and stored at 4°C.

Preparation of liposomes and BNNTP-incorporated liposomes

To prepare the liposomes, we placed 2 mg of lipids dissolved in chloroform into a glass vial. The solvent was then evaporated under an air stream and underwent further drying overnight in a vacuum desiccator. Afterwards, 1 ml of buffer was added to the desiccated lipid film to achieve a final lipid concentration of 2 mg/ml after a 30-s bath sonication. For preparations that incorporated BNNTPs, we first dried BNNTP stock solution in a vacuum desiccator and then rehydrated the resultant BNNTP film with 1 ml of buffer with a 30-s bath sonication. This rehydrated BNNTP solution was then used for hydrating the lipid film with a 30-s bath sonication. The mixtures were then incubated at ambient temperature for 30 min. To facilitate the formation of LUVs or BNNTP-incorporated LUVs (BNNTP-LUVs), we subjected the samples to 7 freeze-thaw cycles, involving rapid freezing in liquid nitrogen and subsequent thawing at 50°C. Afterwards, the samples were extruded through 100- or 200-nm pore-sized polycarbonate membranes 21 times using a mini extruder (Avanti Polar Lipids).

TEM sample preparation

Ten-microliter aliquots of BNNTP stock solution were dispensed onto EMS Holey Carbon–coated 200-mesh copper TEM grids placed on top of quantitative filter paper. The TEM grids were dried overnight in a desiccator. Cryo-TEM samples were prepared by first glow discharge cleaning Quantifoil Holey Carbon support grids with a PELCO easiGlow system. Then, 10-μl aliquots of BNNTP-LUV solution were applied to the cleaned grids in a Gatan Cryoplunge 3 system. Blotting with filter paper and plunging into liquid ethane was handled automatically by the Cryoplunge 3 system. Blotting time varied from 3 to 5 s. Cryo-TEM samples were loaded into a Simple Origin Model 215 cryo transfer holder held below 100 K and inserted into the TEM for cryo-TEM imaging.

TEM imaging and analysis

All imaging was conducted using a JEOL JEM-2100F transmission electron microscope operated at 200 kV. Conventional TEM images were formed using a Gatan ORIUS SC1000 charge-coupled device (CCD) camera at magnifications ranging from ×40,000 to ×1,200,000 with a binning factor of 2. Cryo-TEM images were formed using the ORIUS or Gatan Ultrascan 1000 CCD camera equipped with a Gatan Energy Filter (GIF). The energy filter width was held at 20 eV to improve image contrast and resolution. Images were formed on the ORIUS camera at magnifications between ×30,000 and ×40,000 with no camera binning. Images were formed on the Ultrascan camera with energy filtering at pre-GIF magnifications of between ×5000 and ×6000. In all cases, defocus values ranged from 1 to 2 μm. In-house codes were used for measurements of BNNTP length and membrane insertion angle. Image denoising and contrast enhancement were also performed using an in-house code. As the BNNTP images are two-dimensional projections, the measured lengths represent a lower limit of the true length and inclined angles are not accessible.

HIM imaging

Following 2-min sonication, 10-μl aliquots of BNNT-lipid aqueous solution (uncut tubes) were drop cast onto silicon substrates and dried in air. The HIM imaging was performed at 25 kV using a Zeiss ORION NanoFab multibeam ion microscope using a 0.5-pA He ion beam with a nominal probe diameter of 0.5 nm. Images were acquired using an Everhart-Thornley detector, collecting secondary electrons generated by the scanning ion beam. Typical acquisition parameters were a field of view to 5 to 15 μm, a scan dwell time of 1 μs, a scan size of 2048 × 2048 pixels, and a line average of 8.

AFM imaging and analysis

AFM images were acquired using tapping mode in air on a MultiMode 8, Nanoscope IV system (Bruker) using RTESPA-150 probes (150-kHz nominal frequency and a 5 N/m spring constant) from the

same vendor. For sample preparation, 40 μl of BNNTP stock solution was deposited onto freshly cleaved mica substrates, incubated for 30 min at room temperature, rinsed with DI water, and subsequently dried overnight in a vacuum desiccator. The AFM imaging reliably represented the true height (or diameter) of the BNNTPs.

CF dye leakage assay

For this assay, we prepared ~200-nm-diameter DOPC LUVs using a buffer containing 50 mM 5(6)-CF, 10 mM Hepes, and 100 mM NaCl at pH 7.5. Unencapsulated CF dye was removed using size exclusion chromatography on a Sepharose CL-6B column. We collected 2-ml fractions using a buffer of 10 mM Hepes and 100 mM NaCl at pH 7.5 as the eluent (NaCl buffer). In a typical experiment, 50 μl of the CF-encapsulating LUV suspension was diluted into 2 ml of NaCl buffer to establish a concentration gradient for the CF dye. After ~10 s, a solution of BNNTPs was injected into the suspension under gentle stirring. The fluorescence emission of CF was monitored at a wavelength of 517 nm with an excitation at 492 nm using a fluorometer (FluoroMax-4, Horiba Inc). At around 350 s, a 20-μl solution of 10% v/v Triton X-100 was added to rupture the LUVs and release the dye. The resulting transport trace was quantified by normalizing the fluorescence intensity according to Eq. 1.

$$F_N = \frac{F_t - F_0}{F_1 - F_0} \tag{1}$$

where F_N represents the fractional emission intensity, F_t is the fluorescence intensity at time t, F_1 is the intensity after Triton X-100 addition, and F_0 is the initial fluorescence intensity.

Single-channel recording of BNNTP conductance

BNNTP conductance was evaluated in a DIB setup. Briefly, lipid bilayers were formed between two aqueous droplets immersed in hexadecane oil and lined with the lipid monolayer, using the "lipid in" technique (*32*, *33*). DPhPC LUVs (~100-nm diameter) were prepared in a KCl buffer containing 10 mM tris and 1 mM EDTA. Two 100-μm-diameter Ag/AgCl electrodes with ball-ended tips were made hydrophilic by coating with low-melt agarose in KCl buffer (3% w/v). Electrodes were affixed to micromanipulators (NMN-21, Narishige) mounted onto an inverted optical microscope (Leica DMi1) and connected to a patch-clamp amplifier headstage input and ground. Droplets of LUV solution (~300 nl) were carefully placed on the electrodes in the hexadecane oil bath using a micropipette. After a 5-min incubation, the droplets were gently brought together to form a bilayer. Bilayer formation was confirmed by monitoring membrane capacitance upon application of a triangular voltage waveform. For these experiments, BNNTP stock solutions were first dried, then dispersed in KCl buffer using 5-min bath sonication, and then introduced to the LUV solutions at ~1% v/v concentration just before droplet formation. The insertion of BNNTPs into the lipid bilayers and the associated ion transport were monitored by real-time current measurements under an applied potential range of 100 to 200 mV. As a positive control, the conductance of α-HL was measured using diluted α-HL stock solutions (0.5 mg/ml reduced to 1 μg/ml) in the LUVs for droplet formation. All currents were recorded using an Axopatch 200B patch-clamp amplifier coupled with a 1550B data acquisition system (Molecular Devices), operating at a sampling frequency of 20 kHz and a low band-pass filter frequency of 1 kHz.

DNA translocation measurements

For these experiments, a 50-adenine (50-A) ssDNA was premixed into the BNNTP-LUV solutions, made with 3 M KCl, 10 mM tris, and 1 mM EDTA at pH 7.5, reaching a final concentration of 100 pM. The ssDNA was placed only into the cis droplet of the DIB setup. DNA translocation events were observed by applying a steady 150-mV bias across the bilayer and monitoring the conductance between the droplets at a high sampling frequency of 250 kHz with a low-pass filter set to 1 kHz.

Reversal potential measurements for ion selectivity determination and osmotic power generation

We measured the reversal potential in the DIB setup by using LUV solutions with different KCl concentrations in the two droplets as described in the text. The tips of the Ag/AgCl electrodes were coated with agarose gel matched to the KCl concentration in each droplet. Following the incorporation of BNNTPs, we measured transmembrane current in 10-mV increments to obtain *I*-*V* characteristics and determine zero current voltages. The reversal potential was then calculated by subtracting the theoretical redox potential of the electrodes from these zero current voltages. We computed the theoretical redox potential using the Nernst equation (Eq. 2).

$$V_{\text{redox}} = \frac{RT}{F}\ln\frac{a_{\text{cis}}}{a_{\text{trans}}} \tag{2}$$

where R is the gas constant, T is the temperature of the solutions, F is the Faraday constant, and a is the activity of the ionic species (*35*). The reversal potential value was then converted into the transference number for the BNNTPs (Eq. 3) (*8*, *63*) using the Henderson equation

$$V_{\text{R}} = \left(2t_+ - 1\right)\frac{RT}{F}\ln\frac{a_{\text{cis}}}{a_{\text{trans}}} \tag{3}$$

where V_{R} denotes the measured reversal potential, and t_+ is the K^+ ion transference number. We calculated the K^+/Cl^- ion permselectivity of BNNTPs from transference numbers (Eq. 4).

$$P_{\text{s}} = \frac{t_+ - t_{+\text{bulk}}}{1 - t_{+\text{bulk}}} \tag{4}$$

where P_{s} is the permselectivity, and $t_{+\text{bulk}}$ is the K^+ ion transference number in the bulk solution. Last, the K^+/Cl^- ion SR was determined using Eq. 5.

$$\text{SR} = \frac{t_+}{1 - t_+} \tag{5}$$

The maximum osmotic power (P_{max}) generated by BNNTPs was calculated from the measured values of single BNNTP conductance G at the trans concentration (*12*) and the experimentally determined reversal potential value V_{R} (Eq. 6).

$$P_{\text{max}} = \frac{1}{4}V_{\text{R}}^2 G \tag{6}$$

We calculated the power density ($P_{\text{maxdensity}}$) by normalizing the single pore power to the BNNTP pore area (Eq. 7).

$$P_{\text{maxdensity}} = \frac{4P_{\text{max}}}{\pi d^2} \tag{7}$$

where d is the inner diameter of BNNTPs. The efficiency η_{max} corresponding to the maximum power generation was determined using Eq. 8.

$$\eta_{max} = \frac{\left(2t_+ - 1\right)^2}{2} \quad (8)$$

Supplementary Materials

This PDF file includes:

Figs. S1 to S15

REFERENCES AND NOTES

1. S. Howorka, Building membrane nanopores. *Nat. Nanotechnol.* **12**, 619–630 (2017).
2. J. Xu, D. A. Lavan, Designing artificial cells to harness the biological ion concentration gradient. *Nat. Nanotechnol.* **3**, 666–670 (2008).
3. E. Flood, C. Boiteux, B. Lev, I. Vorobyov, T. W. Allen, Atomistic simulations of membrane ion channel conduction, gating, and modulation. *Chem. Rev.* **119**, 7737–7832 (2019).
4. H. Zhang, X. Li, J. Hou, L. Jiang, H. Wang, Angstrom-scale ion channels towards single-ion selectivity. *Chem. Soc. Rev.* **51**, 2224–2254 (2022).
5. Z. Zhang, L. Wen, L. Jiang, Bioinspired smart asymmetric nanochannel membranes. *Chem. Soc. Rev.* **47**, 322–356 (2018).
6. N. R. Aluru, F. Aydin, M. Z. Bazant, D. Blankschtein, A. H. Brozena, J. P. de Souza, M. Elimelech, S. Faucher, J. T. Fourkas, V. B. Koman, M. Kuehne, H. J. Kulik, H. K. Li, Y. Li, Z. Li, A. Majumdar, J. Martis, R. P. Misra, A. Noy, T. A. Pham, H. Qu, A. Rayabharam, M. A. Reed, C. L. Ritt, E. Schwegler, Z. Siwy, M. S. Strano, Y. Wang, Y. C. Yao, C. Zhan, Z. Zhang, Fluids and electrolytes under confinement in single-digit nanopores. *Chem. Rev.* **123**, 2737–2831 (2023).
7. J. Feng, K. Liu, M. Graf, D. Dumcenco, A. Kis, M. Di Ventra, A. Radenovic, Observation of ionic Coulomb blockade in nanopores. *Nat. Mater.* **15**, 850–855 (2016).
8. J. Feng, M. Graf, K. Liu, D. Ovchinnikov, D. Dumcenco, M. Heiranian, V. Nandigana, N. R. Aluru, A. Kis, A. Radenovic, Single-layer MoS_2 nanopores as nanopower generators. *Nature* **536**, 197–200 (2016).
9. S. Goutham, A. Keerthi, A. Ismail, A. Bhardwaj, H. Jalali, Y. You, Y. Li, N. Hassani, H. Peng, M. V. S. Martins, F. Wang, M. Neek-Amal, B. Radha, Beyond steric selectivity of ions using ångström-scale capillaries. *Nat. Nanotechnol.* **18**, 596–601 (2023).
10. A. Siria, M.-L. Bocquet, L. Bocquet, New avenues for the large-scale harvesting of blue energy. *Nat. Rev. Chem.* **1**, 0091 (2017).
11. Y. Zhang, J. Riexinger, X. Yang, E. Mikhailova, Y. Jin, L. Zhou, H. Bayley, A microscale soft ionic power source modulates neuronal network activity. *Nature* **620**, 1001–1006 (2023).
12. M. Macha, S. Marion, V. V. R. Nandigana, A. Radenovic, 2D materials as an emerging platform for nanopore-based power generation. *Nat. Rev. Mater.* **4**, 588–605 (2019).
13. K. Xiao, L. Jiang, M. Antonietti, Ion transport in nanofluidic devices for energy harvesting. *Joule* **3**, 2364–2380 (2019).
14. R. Arenal, X. Blase, A. Loiseau, Boron-nitride and boron-carbonitride nanotubes: Synthesis, characterization and theory. *Adv. Phys.* **59**, 101–179 (2010).
15. A. Siria, P. Poncharal, A. L. Biance, R. Fulcrand, X. Blase, S. T. Purcell, L. Bocquet, Giant osmotic energy conversion measured in a single transmembrane boron nitride nanotube. *Nature* **494**, 455–458 (2013).
16. E. Secchi, S. Marbach, A. Nigues, D. Stein, A. Siria, L. Bocquet, Massive radius-dependent flow slippage in carbon nanotubes. *Nature* **537**, 210–213 (2016).
17. A. Pendse, S. Cetindag, P. Rehak, S. Behura, H. Gao, N. H. L. Nguyen, T. Wang, V. Berry, P. Král, J. Shan, S. Kim, Highly efficient osmotic energy harvesting in charged boron-nitride-nanopore membranes. *Adv. Funct. Mater.* **31**, 2009586 (2021).
18. S. Cetindag, A. Pendse, R. J. Castellano, P. Rehak, M. Howard, K. Wang, J. Yi, R. F. Praino, P. Kral, L. Liu, Anomalous diffusive and electric-field-driven ion transport in boron-nitride nanotubes. *ChemRxiv* (2023); http://10.26434/chemrxiv-22023-w26482kh.
19. A. Pendse, S. Cetindag, K. Wang, D. Li, R. J. Castellano, D.-C. Yang, T. Wang, J. W. Shan, S. Kim, Intrinsic ion transport of highly charged sub-3-nm boron nitride nanotubes. *Mater. Today* **60**, 79–90 (2022).
20. B. Grosjean, C. Pean, A. Siria, L. Bocquet, R. Vuilleumier, M. L. Bocquet, Chemisorption of hydroxide on 2D materials from DFT calculations: Graphene versus hexagonal boron nitride. *J. Phys. Chem. Lett.* **7**, 4695–4700 (2016).
21. E. Mangaud, M.-L. Bocquet, L. Bocquet, B. Rotenberg, Chemisorbed vs physisorbed surface charge and its impact on electrokinetic transport: Carbon vs boron nitride surface. *J. Chem. Phys.* **156**, 044703 (2022).
22. F. L. Thiemann, C. Schran, P. Rowe, E. A. Muller, A. Michaelides, Water flow in single-wall nanotubes: Oxygen makes it slip, hydrogen makes it stick. *ACS Nano* **16**, 10775–10782 (2022).
23. Z. Zhang, L. Wen, L. Jiang, Nanofluidics for osmotic energy conversion. *Nat. Rev. Mater.* **6**, 622–639 (2021).
24. X. Tong, S. Liu, J. Crittenden, Y. Chen, Nanofluidic membranes to address the challenges of salinity gradient power harvesting. *ACS Nano* **15**, 5838–5860 (2021).
25. L. Cao, F. Xiao, Y. Feng, W. Zhu, W. Geng, J. Yang, X. Zhang, N. Li, W. Guo, L. Jiang, Anomalous channel-length dependence in nanofluidic osmotic energy conversion. *Adv. Funct. Mater.* **27**, 1604302 (2017).
26. J. Geng, K. Kim, J. Zhang, A. Escalada, R. Tunuguntla, L. R. Comolli, F. I. Allen, A. V. Shnyrova, K. R. Cho, D. Munoz, Y. M. Wang, C. P. Grigoropoulos, C. M. Ajo-Franklin, V. A. Frolov, A. Noy, Stochastic transport through carbon nanotubes in lipid bilayers and live cell membranes. *Nature* **514**, 612–615 (2014).
27. L. Liu, C. Yang, K. Zhao, J. Li, H. C. Wu, Ultrashort single-walled carbon nanotubes in a lipid bilayer as a new nanopore sensor. *Nat. Commun.* **4**, 2989 (2013).
28. R. H. Tunuguntla, A. Escalada, V. A. Frolov, A. Noy, Synthesis, lipid membrane incorporation, and ion permeability testing of carbon nanotube porins. *Nat. Protoc.* **11**, 2029–2047 (2016).
29. A. O. Maselugbo, H. B. Harrison, J. R. Alston, Boron nitride nanotubes: A review of recent progress on purification methods and techniques. *J. Mater. Res.* **37**, 4438–4458 (2022).
30. S. Furusawa, Y. Nakanishi, Y. Yomogida, Y. Sato, Y. Zheng, T. Tanaka, K. Yanagi, K. Suenaga, S. Maruyama, R. Xiang, Y. Miyata, Surfactant-assisted isolation of small-diameter boron-nitride nanotubes for molding one-dimensional van der Waals heterostructures. *ACS Nano* **16**, 16636–16644 (2022).
31. J. Shen, Y. Gu, L. Ke, Q. Zhang, Y. Cao, Y. Lin, Z. Wu, C. Wu, Y. Mu, Y. L. Wu, C. Ren, H. Zeng, Cholesterol-stabilized membrane-active nanopores with anticancer activities. *Nat. Commun.* **13**, 5985 (2022).
32. S. Leptihn, O. K. Castell, B. Cronin, E.-H. Lee, L. C. M. Gross, D. P. Marshall, J. R. Thompson, M. Holden, M. I. Wallace, Constructing droplet interface bilayers from the contact of aqueous droplets in oil. *Nat. Protoc.* **8**, 1048–1057 (2013).
33. H. Bayley, B. Cronin, A. Heron, M. A. Holden, W. L. Hwang, R. Syeda, J. Thompson, M. Wallace, Droplet interface bilayers. *Mol. Biosyst.* **4**, 1191–1208 (2008).
34. G. Maglia, A. J. Heron, W. L. Hwang, M. A. Holden, E. Mikhailova, Q. Li, S. Cheley, H. Bayley, Droplet networks with incorporated protein diodes show collective properties. *Nat. Nanotechnol.* **4**, 437–440 (2009).
35. W. M. Haynes, *CRC Handbook of Chemistry and Physics* (CRC Press, 2016).
36. E. Secchi, A. Nigues, L. Jubin, A. Siria, L. Bocquet, Scaling behavior for ionic transport and its fluctuations in individual carbon nanotubes. *Phys. Rev. Lett.* **116**, 154501 (2016).
37. Y.-C. Yao, A. Taqieddin, M. A. Alibakhshi, M. Wanunu, N. R. Aluru, A. Noy, Strong electroosmotic coupling dominates ion conductance of 1.5 nm diameter carbon nanotube porins. *ACS Nano* **13**, 12851–12859 (2019).
38. D. Stein, M. Kruithof, C. Dekker, Surface-charge-governed ion transport in nanofluidic channels. *Phys. Rev. Lett.* **93**, 035901 (2004).
39. M. Manghi, J. Palmeri, K. Yazda, F. Henn, V. Jourdain, Role of charge regulation and flow slip in the ionic conductance of nanopores: An analytical approach. *Phys. Rev. E* **98**, 012605 (2018).
40. M. Queralt-Martin, M. L. Lopez, M. Aguilella-Arzo, V. M. Aguilella, A. Alcaraz, Scaling behavior of ionic transport in membrane nanochannels. *Nano Lett.* **18**, 6604–6610 (2018).
41. G. Cui, Z. Xu, H. Li, S. Zhang, L. Xu, A. Siria, M. Ma, Enhanced osmotic transport in individual double-walled carbon nanotube. *Nat. Commun.* **14**, 2295 (2023).
42. Y. Noh, N. R. Aluru, Ion transport in electrically imperfect nanopores. *ACS Nano* **14**, 10518–10526 (2020).
43. T. Emmerich, K. S. Vasu, A. Nigues, A. Keerthi, B. Radha, A. Siria, L. Bocquet, Enhanced nanofluidic transport in activated carbon nanoconduits. *Nat. Mater.* **21**, 696–702 (2022).
44. R. H. Tunuguntla, R. Y. Henley, Y. C. Yao, T. A. Pham, M. Wanunu, A. Noy, Enhanced water permeability and tunable ion selectivity in subnanometer carbon nanotube porins. *Science* **357**, 792–796 (2017).
45. Z. Li, Y. Qiu, Y. Zhang, M. Yue, Y. Chen, Effects of surface trapping and contact ion pairing on ion transport in nanopores. *J. Phys. Chem. C* **123**, 15314–15322 (2019).
46. M. D. B. Pérez, A. Nicolaï, P. Delarue, V. Meunier, M. Drndić, P. Senet, Improved model of ionic transport in 2-D MoS_2 membranes with sub-5 nm pores. *Appl. Phys. Lett.* **114**, 023107 (2019).
47. J. Ma, K. Li, Z. Li, Y. Qiu, W. Si, Y. Ge, J. Sha, L. Liu, X. Xie, H. Yi, Z. Ni, D. Li, Y. Chen, Drastically reduced ion mobility in a nanopore due to enhanced pairing and collisions between dehydrated ions. *J. Am. Chem. Soc.* **141**, 4264–4272 (2019).
48. N. Kavokine, S. Marbach, A. Siria, L. Bocquet, Ionic Coulomb blockade as a fractional Wien effect. *Nat. Nanotechnol.* **14**, 573–578 (2019).
49. R. M. Lynden-Bell, J. C. Rasaiah, Mobility and solvation of ions in channels. *J. Chem. Phys.* **105**, 9266–9280 (1996).
50. S. Luo, R. P. Misra, D. Blankschtein, Water electric field induced modulation of the wetting of hexagonal boron nitride: Insights from multiscale modeling of many-body polarization. *ACS Nano* **18**, 1629–1646 (2024).
51. Y. Guo, M. Werner, R. Seemann, V. A. Baulin, J. B. Fleury, Tension-induced translocation of an ultrashort carbon nanotube through a phospholipid bilayer. *ACS Nano* **12**, 12042–12049 (2018).
52. A. Meller, L. Nivon, E. Brandin, J. Golovchenko, D. Branton, Rapid nanopore discrimination between single polynucleotide molecules. *Proc. Natl. Acad. Sci. U.S.A.* **97**, 1079–1084 (2000).

53. S. Marbach, L. Bocquet, Osmosis, from molecular insights to large-scale applications. *Chem. Soc. Rev.* **48**, 3102–3144 (2019).
54. L. Q. Gu, M. Dalla Serra, J. B. Vincent, G. Vigh, S. Cheley, O. Braha, H. Bayley, Reversal of charge selectivity in transmembrane protein pores by using noncovalent molecular adapters. *Proc. Natl. Acad. Sci. U.S.A.* **97**, 3959–3964 (2000).
55. E. M. Nestorovich, T. K. Rostovtseva, S. M. Bezrukov, Residue ionization and ion transport through OmpF channels. *Biophys. J.* **85**, 3718–3729 (2003).
56. E. García-Giménez, A. Alcaraz, V. M. Aguilella, P. Ramírez, Directional ion selectivity in a biological nanopore with bipolar structure. *J. Membr. Sci.* **331**, 137–142 (2009).
57. Y. Zhu, H. G. Derami, P. Gupta, R. Gupta, S. Singamaneni, Y.-S. Jun, Ionic surface propensity controls pH in nanopores. *Chem* **8**, 3081–3095 (2022).
58. H. N. Po, N. M. Senozan, The Henderson-Hasselbalch equation: Its history and limitations. *J. Chem. Educ.* **78**, 1499 (2001).
59. T. Xu, K. Zhang, Q. Cai, N. Wang, L. Wu, Q. He, H. Wang, Y. Zhang, Y. Xie, Y. Yao, Y. Chen, Advances in synthesis and applications of boron nitride nanotubes: A review. *Chem. Eng. J.* **431**, 134118 (2022).
60. M. B. Jakubinek, K. S. Kim, M. J. Kim, A. A. Martí, M. Pasquali, Recent advances and perspective on boron nitride nanotubes: From synthesis to applications. *J. Mater. Res.* **37**, 4403–4418 (2022).
61. L. Wang, Z. Wang, S. K. Patel, S. Lin, M. Elimelech, Nanopore-based power generation from salinity gradient: Why it is not viable. *ACS Nano* **15**, 4093–4107 (2021).
62. S. Lin, Z. Wang, L. Wang, M. Elimelech, Salinity gradient energy is not a competitive source of renewable energy. *Joule* **8**, 334–343 (2024).
63. D.-K. Kim, C. Duan, Y.-F. Chen, A. Majumdar, Power generation from concentration gradient by reverse electrodialysis in ion-selective nanochannels. *Microfluid. Nanofluidics* **9**, 1215–1224 (2010).

Acknowledgments: We thank BNNT, LLC. for providing BNNT source material. Work at the Lawrence Livermore National Laboratory was performed under the auspices of the US Department of Energy under contract DE-AC52-07NA27344. **Funding:** BNNTP synthesis and transport studies were supported by the US Department of Energy, Office of Basic Energy Sciences, Division of Materials Science and Engineering under award no. SCW1607 at the Lawrence Livermore National Laboratory (LLNL). HR-TEM and cryo-TEM studies have been supported as part of the Center for Enhanced Nanofluidic Transport (CENT), an Energy Frontier Research Center funded by the US Department of Energy, Office of Science, Basic Energy Sciences under Award no. DE-SC0019112. HIM imaging at the qb3 Biomolecular Nanotechnology Center at UC Berkeley was supported by the National Science Foundation under award no. 2110924. **Author contributions:** Z.L. and A.N. designed the experiments and wrote the paper. Z.L. and Y.L. synthesized BNNTPs. Z.L. performed transport experiments. A.T.H. and J.C. performed TEM experiments. Y.W. performed AFM experiments. D.O.B. and F.I.A. performed HIM experiments. L.R.S. and R.R.W. synthesized BNNT source material. All authors commented on the results and participated in the editing of the manuscript. **Competing interests:** R.R.W. is President, including equity interest, and L.R.S. is the Product Development Manager at BNNT Materials, LLC, which has commercialized the synthesis of boron nitride nanotubes. The remaining authors declare that they have no competing interests. **Data and materials availability:** All data needed to evaluate the conclusions in the paper are present in the paper and/or the Supplementary Materials. All data presented in this work also have been deposited to Figshare and are available at DOI:10.6084/m9.figshare.25271002.

Submitted 28 February 2024
Accepted 1 August 2024
Published 6 September 2024
10.1126/sciadv.ado8081